5-2015

Ultrasonic thickness structural health monitoring photoelastic visualization and measurement accuracy for internal pipe corrosion

Thomas J. Eason
Iowa State University, easont@iastate.edu

Leonard J. Bond
Iowa State University, bondlj@iastate.edu

Mark G. Lozev
BP Products North America

Ultrasonic thickness structural health monitoring photoelastic visualization and measurement accuracy for internal pipe corrosion

Abstract
Oil refinery production of fuels is becoming more challenging as a result of the changing world supply of crude oil towards properties of higher density, higher sulfur concentration, and higher acidity. One such production challenge is an increased risk of naphthenic acid corrosion that can result in various surface degradation profiles of uniform corrosion, non-uniform corrosion, and localized pitting in piping systems at temperatures between 150°C and 400°C. The irregular internal surface topology and high external surface temperature leads to a challenging in-service monitoring application for accurate pipe wall thickness measurements. Improved measurement technology is needed to continuously profile the local minimum thickness points of a non-uniformly corroding surface. The measurement accuracy and precision must be sufficient to provide a better understanding of the integrity risk associated with refining crude oils of higher acid concentration. This paper discusses potential technologies for measuring localized internal corrosion in high temperature steel piping and describes the approach under investigation to apply flexible ultrasonic thin-film piezoelectric transducer arrays fabricated by the sol-gel manufacturing process. Next, the elastic wave beam profile of a sol-gel transducer is characterized via photoelastic visualization. Finally, the variables that impact measurement accuracy and precision are discussed and a maximum likelihood statistical method is presented and demonstrated to quantify the measurement accuracy and precision of various time-of-flight thickness calculation methods in an ideal environment. The statistical method results in confidence values analogous to the a90 and a90/95terminology used in Probability-of-Detection (POD) assessments.

Disciplines
Oil, Gas, and Energy | Structures and Materials

Comments
This paper is from *Proc. SPIE* 9439, Smart Materials and Nondestructive Evaluation for Energy Systems 2015, 94390M (March 27, 2015); doi:10.1117/12.2084223. Posted with permission.

Ultrasonic Thickness Structural Health Monitoring Photoelastic Visualization and Measurement Accuracy for Internal Pipe Corrosion

Thomas J. Eason*[ab], Leonard J. Bond[a], Mark G. Lozev[b]
[a]Center for Nondestructive Evaluation, Iowa State University, 1915 Scholl Rd., Ames, IA, 50011;
[b]BP Products North America, Refining & Logistics Technology, 150 W. Warrenville Rd., Naperville, IL 60563

ABSTRACT

Oil refinery production of fuels is becoming more challenging as a result of the changing world supply of crude oil towards properties of higher density, higher sulfur concentration, and higher acidity. One such production challenge is an increased risk of naphthenic acid corrosion that can result in various surface degradation profiles of uniform corrosion, non-uniform corrosion, and localized pitting in piping systems at temperatures between 150°C and 400°C. The irregular internal surface topology and high external surface temperature leads to a challenging in-service monitoring application for accurate pipe wall thickness measurements. Improved measurement technology is needed to continuously profile the local minimum thickness points of a non-uniformly corroding surface. The measurement accuracy and precision must be sufficient to provide a better understanding of the integrity risk associated with refining crude oils of higher acid concentration. This paper discusses potential technologies for measuring localized internal corrosion in high temperature steel piping and describes the approach under investigation to apply flexible ultrasonic thin-film piezoelectric transducer arrays fabricated by the sol-gel manufacturing process. Next, the elastic wave beam profile of a sol-gel transducer is characterized via photoelastic visualization. Finally, the variables that impact measurement accuracy and precision are discussed and a maximum likelihood statistical method is presented and demonstrated to quantify the measurement accuracy and precision of various time-of-flight thickness calculation methods in an ideal environment. The statistical method results in confidence values analogous to the a_{90} and $a_{90/95}$ terminology used in Probability-of-Detection (POD) assessments.

Keywords: corrosion, structural health monitoring, ultrasonic thickness, high temperature, thin-film transducer, sol-gel, photoelastic, measurement accuracy

1. INTRODUCTION

The ability of online measurement technology to characterize non-uniform and localized pitting corrosion degradation at elevated temperatures could be improved. This paper looks to review the various Non-Destructive Evaluation (NDE) measurement techniques, describe a sol-gel ultrasonic sensor material technology that may able to characterize high temperature localized corrosion, begin characterizing sol-gel transducers via photoelastic visualization, and apply a maximum likelihood statistical method to quantify the measurement accuracy and precision of various thickness calculation methods in an ideal environment.

Oil refinery production of high quality clean fuels is becoming more challenging as a result of the changing world supply of crude oil towards properties of higher density, higher sulfur concentration, and higher acidity[1]. One such production challenge is an increased risk of corrosion from crudes with a high concentration of naphthenic acids[2]. The rate of naphthenic acid corrosion (NAC) is considered to be dependent on metallurgy, acid species, acid concentration, sulfur concentration, process temperature, shear stress, and the extent of a gas phase[3] resulting in a corrosion rate that is difficult to predict. The degradation morphology of NAC can be localized pitting at temperatures between 150°C and 400°C[4] resulting in challenging in-service inspection. Varying the acid concentration, flow rate, and temperature can result in three distinct damage mechanisms of uniform, non-uniform, and localized pitting[5].

*easont@iastate.edu; phone 1 515 294-8152; fax 1 515 294-7771; cnde.iastate.edu

Smart Materials and Nondestructive Evaluation for Energy Systems 2015, edited by Norbert G. Meyendorf,
Proc. of SPIE Vol. 9439, 94390M · © 2015 SPIE · CCC code: 0277-786X/15/$18 · doi: 10.1117/12.2084223

1.1 Measurement Requirements

The ideal measurement technology should satisfy two distinct, but related objectives. The first objective is to collect a high frequency of *relative* wall thickness measurements in order to help predict future *corrosion rates*. The relative changes in wall thickness can be correlated with current operational parameters to improve prognostic models resulting in a better prediction of future corrosion rates under future operational conditions. A permanently installed Structural Health Monitoring (SHM) measurement technology may be well suited to provide such high frequency relative thickness measurements.

The second objective is to find and precisely measure the *absolute* thinnest points in a system to perform a *current state* "Fit-for-service"[6] assessment based on the mechanical design, current dimensions, and current operation conditions. A non-permanent manual Non-Destructive Evaluation (NDE) measurement technology may be we suited to provide a more random sampling of precise thickness measurements over a larger surface area in an attempt to find the thinnest points, but access costs can limit the practical frequency of such manual NDE measurements.

The ideal measurement approach should look to incorporate the positive aspects of both SHM and NDE via improved technology and/or intelligently merging SHM into ongoing NDE activities. For the specific case of naphthenic acid corrosion, a list of potential target technology design parameters to address both relative and absolute measurement requirements is shown in Table 1.

Table 1. Potential target technology design parameters for naphthenic acid corrosion monitoring.

Parameter	Potential Target
Temperature	up to 400°C
Thickness Precision	0.05mm
Spatial Resolution Precision	0.05mm width & 0.05mm length
Pipe Wall Thickness	3-25mm
Pipe Diameter	>100mm
Metallurgy	Low-Alloy Steel (<9%Cr & <2.5% Mo)

1.2 Potential Nondestructive Evaluation Methods

The most common practice for corrosion monitoring in piping systems is periodic manual bulk wave ultrasonic thickness measurement. In an effort to assess the state of art and identify potential improvements in measurement capability, prior reviews of inspection technology for corrosion[7] and pipe systems[8-10] as well as general NDE sources[11-12] are referenced.

Optical methods include Endoscopy and Fiber Bragg Gratings. Endoscopic techniques such as Close Circuit Television (CCTV) or boroscope inspection can capture internal pipe surface images as qualitative information. Quantitative 3D topography information and defect characterization can be obtained using various optical equipment configurations mounted on a crawler inside a pipe such as visual odometry[13] or laser ring triangulation[14]. Fiber Bragg Gratings can sense an environmental change in temperature and strain[15]. Strain measurements are proposed to detect an increase in hoop (circumferential) stress as the result of wall thinning due to corrosion in a pipeline[16].

Electromagnetic methods include Remote Field Eddy Current and Pulsed Eddy Current. The Remote Field Eddy Current method applies two magnetizing coils inside a pipe to measure the phase lag which is then correlated to wall thickness. The Pulsed Eddy Current method applies electromagnetic pulses onto the outer pipe surface to induce eddy currents that rapidly decay at the inside surface. The voltage induced by the eddy currents can be measured as a function of time and then correlated to wall thickness based on the point at which rapid signal decay occurs.

Radiographic methods involve the transmission, propagation, attenuation, measurement, and interpretation of energy from a source, through an object, and onto a film or detection device. The intensity of a beam of radiation exiting a material exponentially decays with material thickness based on a linear attenuation coefficient. The individual grains of Traditional Film react and darken with radiation exposure. Computed Radiography methods involve flexible imaging plates that can be digitally scanned and then reused via a photo-stimulable phospors storage process. Digital Radiography methods involve flat panel detectors composed of scintillating material arrays and thin film transistors to display an image at the same time that radiation is passing through an object.

Acoustic emission methods involve the generation of elastic waves (acoustic emissions) as a result of a slight structural deformations. Acoustic measurements are compared to an initial baseline environmental noise measurement. Relatively low amplitude changes from the baseline can be attributed to chemical reactions related to corrosion or the removal of corrosion products from a surface.

Ultrasonic methods involve the transmission and measured reception of elastic wave displacements using a wide range of possible system configurations as previously described[10] involving Bulk and Guided Wave propagation modes as well as piezoelectric, electromagnetic acoustic, magnetostrictive, and laser transduction methods. Periodic bulk wave thickness measurement involving a transducer manually coupled to the outside of a pipe is the most common practice for corrosion monitoring. The thickness of the pipe wall can be determined from the time difference in transducer excitation and reception from a back-wall echo. The received voltage signal can be processed using various filtering and envelope wrapping techniques and analyzed using various time-of-flight calculation methods that can result in slightly different thickness measurement values[17-18].

Table 2. Potential application of various nondestructive evaluation methods. Low potential = o. Moderate potential = +/o. High potential +.

Technique	Sub-technique	Potential for 400°C Surface Temperature	Potential for Permanent Monitoring	Potential for Direct Thickness Measurement	Potential for Localized Measurement
Optical	Endoscopy	o	o	o	+
	Fiber Bragg Grating	+	+	o	o
Electromagnetic	Remote Field Eddy Current	o	o	+	+/o
	Pulsed Eddy Current	+	+	+	+
Radiographic	Traditional Film	+	o	+/o	+
	Computed Radiography	+	o	+/o	+
	Digital Radiography	+	+/o	+/o	+
Acoustic Emission		+	+	o	o
Ultrasonic	Bulk Wave Mode	+	+	+	+
	Guided Wave Mode	+	+	o	o
	Piezoelectric Transduction	+	+	+	+
	Electromagnetic Acoustic Transduction	+/o	+	+	+
	Magnetostrictive Transduction	+/o	+	+	+
	Laser Transduction	+	+/o	+	+

The described methods are summarized in Table 2 for comparison. The temperature characteristic is based on material properties and required access proximity; for example, radiographic techniques do not require direct contact with the pipe surface and can be applied at high temperatures. The permanent monitoring characteristic is based on implementation; for example, endoscopic techniques require line of sight access to the internal pipe surface and are not well suited for in-service online monitoring. The direct thickness measurement characteristic address the physical parameter being measured; for example, acoustic emission specifies an average corrosion rate which can then be used to infer a wall thickness as opposed to directly measuring wall thickness in a bulk wave time-of-flight method. The

potential for localized measurement is with the intention of being able to measure wall thickness in a specific and localized location; for example, fiber Bragg gratings may provide an average wall thickness of a relatively large area.

Permanently installed piezoelectric ultrasonic bulk wave sensors appear to be a relatively good choice to monitor wall thickness of localized high temperature corrosion. Various wave mode, frequency, footprint, and coupling designs are possible and commercially available above ambient temperatures as described in Table 3[19-23].

Table 3. Commercially available permanently installed bulk wave sensors.

Commercial Sensor	Design Temperature	Wave Mode Configuration	Footprint	Coupling
Cosasco Ultracorr	85°C	Compression Pulse-Echo	Single Element 30mm Diameter	Epoxy
GE LT Rightrax	120°C	8.0 MHz Compression Pulse-Echo	14 Element Linear Array 200mm x 12mm	Epoxy
GE HT Rightrax	250°C	5.0 MHz Compression Pulse-Echo	Single Element 7-21mm Diameter	Metal Foil
Permasense WT100	600°C	~2 MHz Shear Horizontal Pitch-Catch	Single Element ~15mm x ~3mm	Dry

1.3 Thin-Film Sol-Gel Transducers

The sol-gel ceramic fabrication process can be applied to produce the piezoelectric material[24] used in thin-film ultrasonic transducers for bulk wave wall thickness measurements[25]. This transducer design has the potential to provide a strong and reliable permanent acoustic bond to the pipe wall surface, has customizable sensor element configurations and dimensions to expand into larger areas of measurement coverage, and also has the potential for installation in high temperature environment[26]. The characterization of such sol-gel transducers and the quantification of measurement accuracy and precision are discussed in the following sections.

2. PHOTOELASTIC VISUALIZATION METHODOLOGY

Elastic wave propagation can be visualized in a transparent material by observing polarized light refracted from pressure gradients via the schlieren method[27], or from localized regions of stress via the photoelastic method. While the schlieren method can be more sensitive to acoustic waves in liquids, the photoelastic method can observe the shear stress mode and is the method applied in this study. The earliest publication of the photoelastic method[28] occurred decades prior to the first applications to ultrasonic visualization[29-32]. More current efforts around image digitization and quantification[33-37] are in part a result of improved camera and LED light source technology. The photoelastic imaging system described in Fig. 1[38] was used for this study.

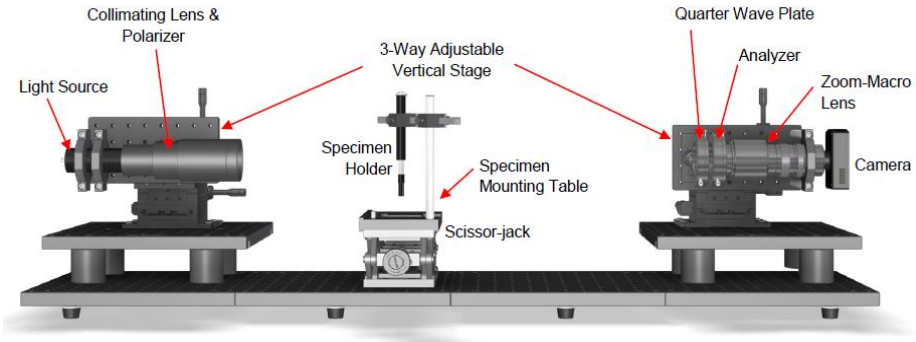

Figure 1. Photoelastic imaging equipment schematic.[38]

3. PHOTOELASTIC VISUALIZATION IMAGES

The elastic wave propagation profiles from a manual ultrasonic contact transducer as well as from a thin-file sol-gel ultrasonic transducer were characterized using photoelastic visualization.

3.1 Manual Contact Transducer

To provide reference images for comparison with a sol-gel transducer, a 5.0 MHz flat 6.35 mm circular Panametrics V110 [Serial #61566] manual ultrasonic contact transducer was investigated. This transducer frequency is common for manual wall thickness measurements of steel pipe. The transducer was applied to a 19 x 65 x 110 mm soda lime glass block with Soundsafe® ultrasonic couplant and a dead weight contact pressure of approximately 9 kPa. The transducer was excited with a 120V square wave at 5.0 MHz frequency. The strobe delay was adjusted to capture photoelastic images at various points in time of the initial beam propagation. The individual images are analogous to a single frame of a beam propagation video. A sampling of four frames are shown in Fig. 2. The primary compression mode as well as the edge effect shear mode waves are observable with color intensity proportional to acoustic amplitude; lighter color correlating to positive amplitude and darker color correlating to negative amplitude.

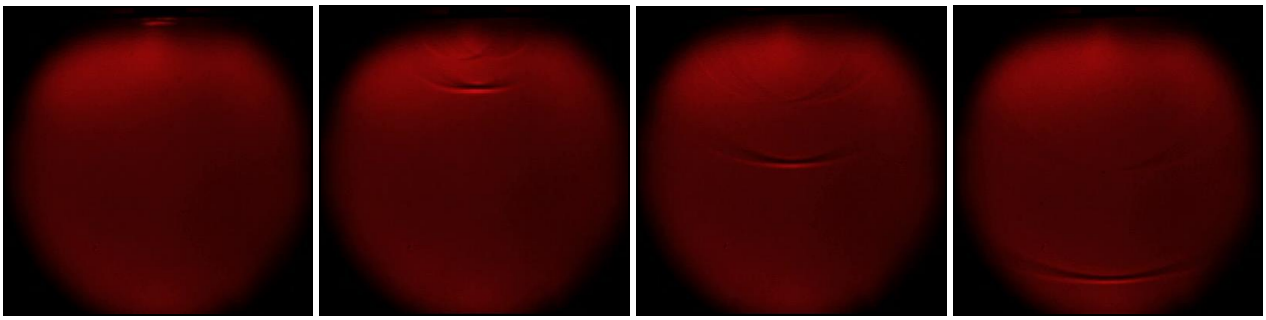

Figure 2. Sequential photoelastic images of wave propagation from a 5.0 MHz Panametrics V110 manual transducer.

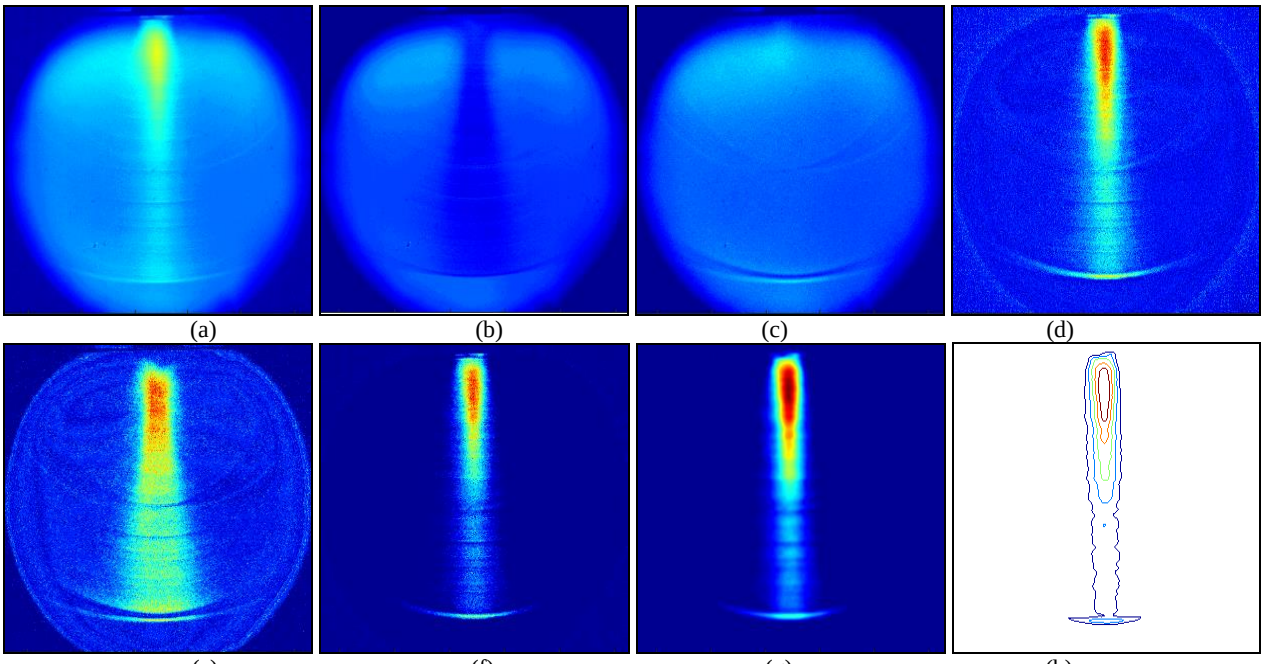

Figure 3. Beam profile construction of a 5.0 MHz Panametrics V110 manual transducer a) maximum spatial amplitude, b) minimum spatial amplitude, c) final frame image, d) normalized maximum amplitude, e) normalized minimum amplitude, f) filtered normalized maximum amplitude, g) filtered smoothed normalized maximum amplitude, and h) isosurface plot.

The photoelastic image frames can be processed to generate the maximum absolute amplitude beam profile as described in Fig. 3. The maximum and minimum pixel values are identified in each frame for each spatial coordinate in Figs. 3a & 3b. The final frame in Fig. 3c is used to normalize the maximum and minimum amplitude images in Figs. 3d & 3e. The normalized maximum amplitude image is then filtered to remove noise below an arbitrary constant value of 4 as shown in Fig. 3f. The normalized and filtered maximum amplitude image is then smoothed with a 2D convolution function applying a 3x3 [.05 .1 .05; .1 .4 .1; .05 .1 .05] smoothing matrix at 100 iterations as shown in Fig. 3g. An isosurface plot is shown in Fig. 3h analogous to a region of focus defined by a dB threshold.

3.2 Thin Film Sol-Gel Transducer

A proprietary 7.5 MHz flat 4mm x 4mm square ultrasonic thin film sol-gel transducer with a 55% -6 dB bandwidth was investigated. The transducer was applied to thin stainless steel film which was then coupled to the same glass block with the same couplant and a dead weight contact pressure of approximately 3 kPa. The transducer was excited with a 120V square wave at 7.5 MHz frequency. A sampling of frames are shown in Fig. 4. The color intensity change is much less obvious making it difficult to identify the primary compression mode.

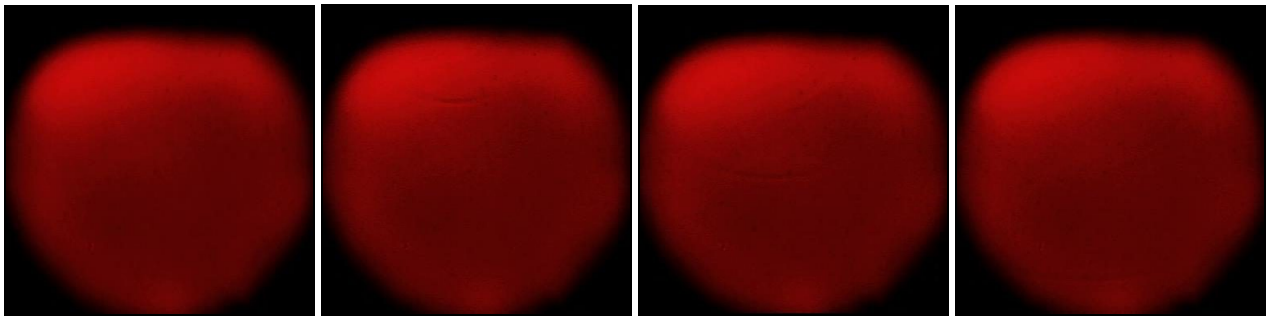

Figure 4. Sequential photoelastic images of wave propagation from a proprietary 7.5 MHz thin film sol-gel transducer.

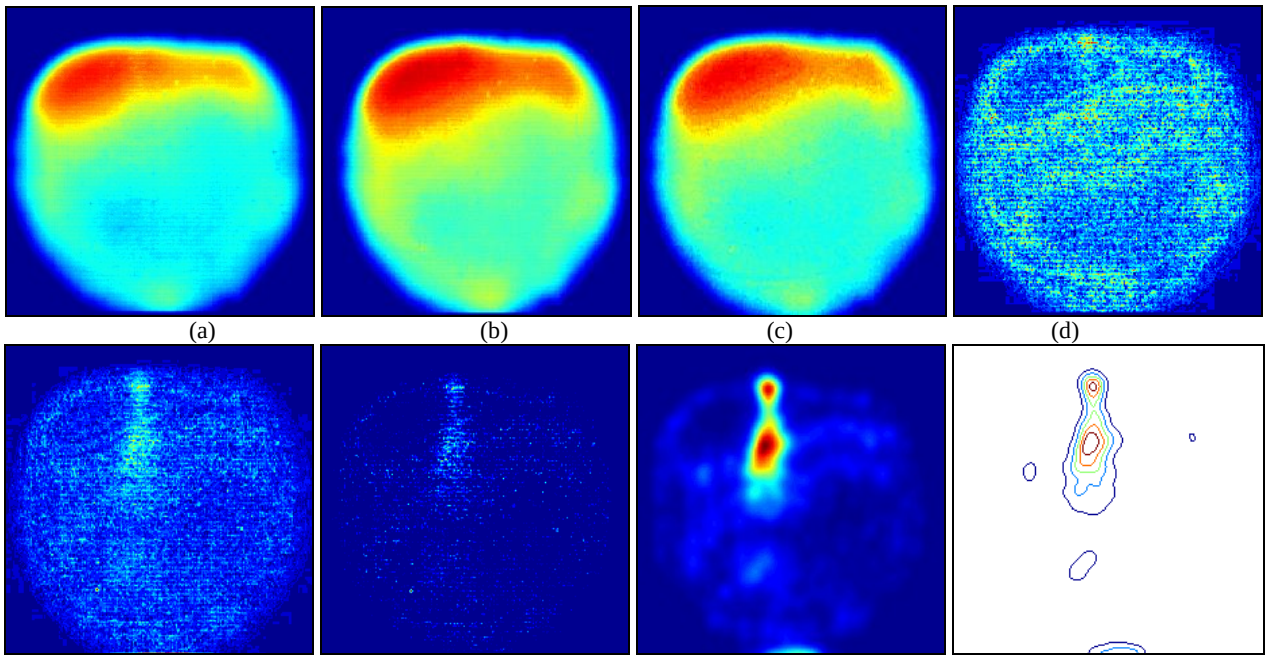

Figure 5. Beam profile construction of a proprietary 7.5 MHz thin film sol-gel transducer a) maximum spatial amplitude, b) minimum spatial amplitude, c) final frame image, d) normalized maximum amplitude, e) normalized minimum amplitude, f) filtered normalized minimum amplitude, g) filtered smoothed normalized minimum amplitude, and h) isosurface plot.

The photoelastic image frames can again be processed to generate the maximum absolute amplitude beam profile as described in Fig. 5. The maximum and minimum pixel values are identified in each frame for each spatial coordinate in Figs. 5a & 5b. The final frame in Fig. 5c is used to normalize the maximum and minimum amplitude images in Figs. 5d and 5e. The normalized minimum amplitude image is then filtered to remove noise below an arbitrary constant value of 3.5 as shown in Fig. 5f. The normalized and filtered minimum amplitude image is then smoothed with a 2D convolution function applying a 3x3 [.05 .1 .05; .1 .4 .1; .05 .1 .05] smoothing matrix at 100 iterations as shown in Fig. 5g. An isosurface plot is shown in Fig. 5h analogous to a region of focus defined by a dB threshold.

4. PHOTOELASTIC VISUALIZATION RESULTS

This section compares the photoelastic beam profile characteristics to other methods.

4.1 Manual Contact Transducer

The classical normalized near field length equation is described in Eq. 1[39], with N_0 as the normalized near field, D as the transducer diameter, f as the acoustic frequency, and c as the wave speed. For the 5.0 MHz flat 6.35 mm circular Panametrics V110 [serial #61566] manual ultrasonic contact transducer: D = 6.35mm, f = 5 MHz, and c = 5840 m/s in soda-lime glass resulting in a near field length of 8.6 mm.

$$N_0 = \frac{D^2 f}{4c} \tag{1}$$

The transduction beam profile was modeled with commercially available CIVA® software that simulates elastodynamic wave propagation behavior based on electromagnetic wave theory[40]. The model configuration is shown in Fig. 6 with a soda lime glass block specimen of 110 mm x 19 mm x 65 mm with density of 2.24 g/cm^3, longitudinal wave speed of 5840 m/s, a transverse wave speed of 2460 m/s, no roughness, and no attenuation. The manual contact transducer was modeled as a single circular 6.35 mm diameter contact transducer with flat focus and a Gaussian frequency spectrum centered at 5 MHz with 100% bandwidth at -6 dB. The inspection was established with a water couplant with a density of 1 gm/cm^3 and a longitudinal wave speed = 1485 m/s. The simulation was run as a 3D computation in a 2D zone scaled to match the photoelastic imaging window and with a uniform 0.5 mm spatial resolution.

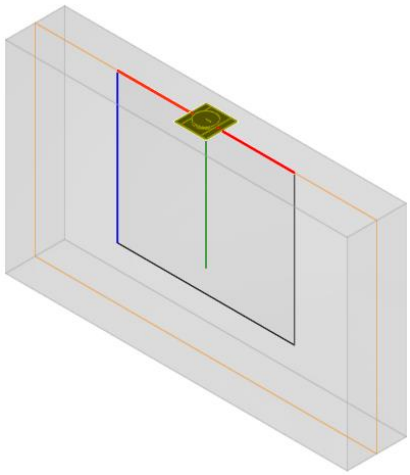

Figure 6. Elastodynamic wave propagation model specimen and transducer configuration.

The modeling results are shown in Fig. 7a with the transducer diameter and calculated near field length shown; a comparison to the equivalent photoelastic generation beam profile is shown in Fig. 7b. The transduction beam profile from the classical equation, elastodynamic simulation, and photoelastic image match relatively well.

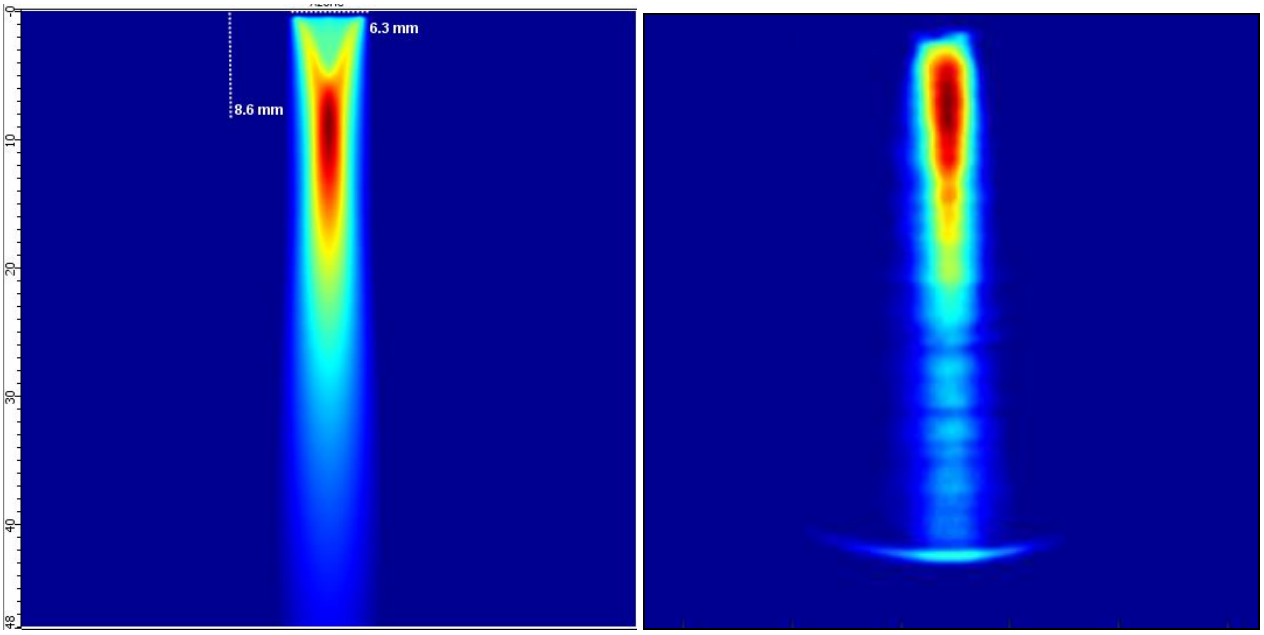

(a) (b)

Figure 7. Comparison of transduction beam profile of manual contact transducer using a) elastodynamic wave CIVA® simulation[40] and b) a reconstruction from photoelastic imaging frames. The length scale [mm] is equally proportional.

4.2 Thin Film Sol-Gel Transducer

Applying Eq. 1 to the proprietary 7.5 MHz thin film sol-gel transducer: D = 4.0 m, f = 7.5 MHz, and c = 5840 m/s results in a near field length of 5.0 mm. The same elastodynamic simulation parameters from the manual contact transducer are used except with a single element 4 mm x 4 mm rectangular contact transducer with flat focus and a Gaussian frequency spectrum centered at 7.5 MHz with 100% bandwidth at -6 dB.

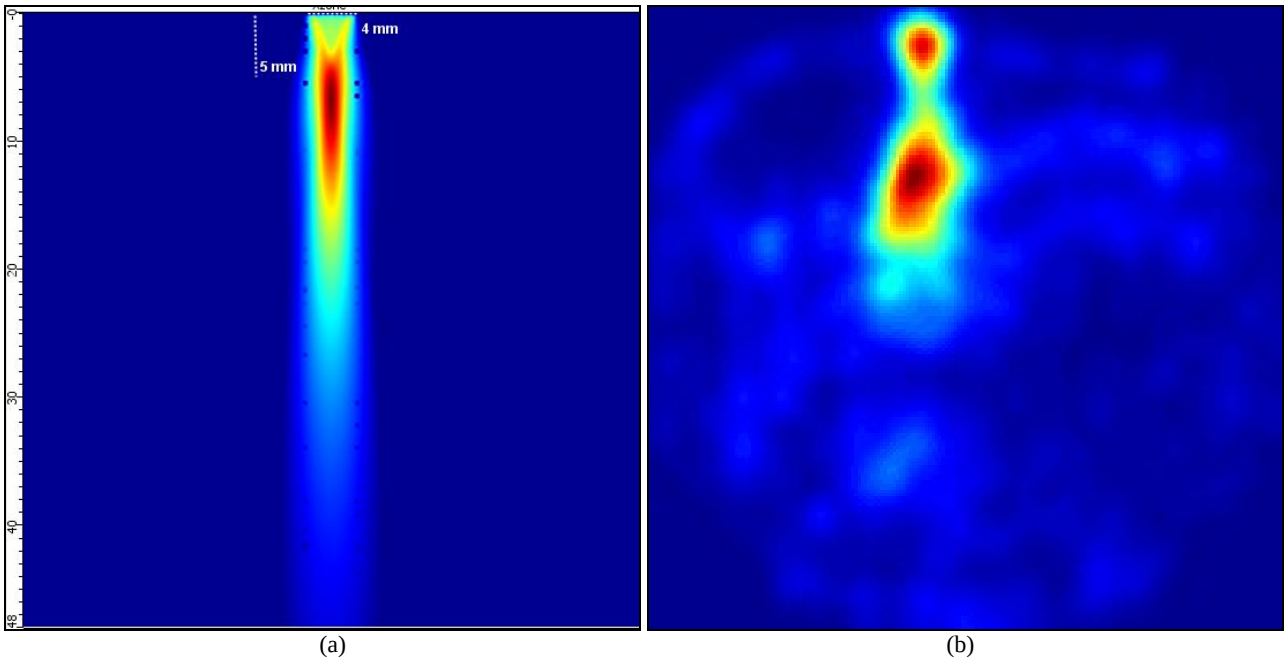

(a) (b)

Figure 8. Comparison of transduction beam profile of thin film sol-gel transducer using a) elastodynamic wave CIVA® simulation[40] and b) a reconstruction from photoelastic imaging frames. The length scale [mm] is equally proportional.

The modeling results are shown in Fig. 8a with the transducer diameter and calcuated near field length shown; a comparison to the equivalent photoelastic generation beam proifile is shown in Fig. 8b. The beam profile from the classical equation and elastodynamic simulation match well, however the photoelastic image does not match well. This is likely a limitation of the photoelastic image measurement being unable to distinguish the beam profile from the variable background noise. This region of higher background noise observed at the top of the image in Fig 5c appears to coincide inversely with the beam profile void observed in Fig 8b. Additional work is necessary to improve light source alignment, optimize lens orientations, increase coupling force, and investigate other sol-gel sensors of larger area in an attempt to better visualize the elastic wave propagation behaviour from a sol-gel transducer.

5. MEASUREMENT ACCURACY METHODOLOGY

A previously reported experiment by Eason et al.[10] was conducted to demonstrate a statistical modeling approach to compare measurement accuracy of multiple bulk wave ultrasonic thickness calculation methods: a local maxima method (Peak-to-Peak), a threshold method (Zero Crossing), and an optimum correlation method (Cross Correlation)[10,17] were investigated.

A total of forty four sol-gel sensor elements were directly deposited[24-25] in 2 x 2 array groups onto a flat step calibration block with a 0.10 ± 0.005 mm step size from 3.00 mm to 4.00 mm as shown in Fig. 9. The elements have an average center frequency of 13.1 MHz and an average bandwidth of 63% at -6 dB. The gain for each element was individually adjusted to maximize the first back-wall reflection amplitude without saturation. A total of thirty seven pulse-echo waveforms were collected for each of the sensor elements over a period of ninety minutes at constant ambient temperature. The first and second signal gates were established to be identical in terms of height, location, and width for all 1628 waveforms. A negative amplitude gate height was used due to the signal asymmetry.

The thirty seven thickness measurements over time were averaged for each sensor element for each of the three methods for a range of acoustic velocity values between 5870 and 5930 m/s. These time average thickness measurements were subtracted from the step calibration block true thickness to produce residual thickness values for each velocity value for each method and for each element. These residual thickness values for the forty four elements were averaged, with outliers excluded. The absolute residual thickness was minimized using a least squared regression to find the ideal velocity for each method. The average velocity among all three methods was 5905 ± 10 m/s.

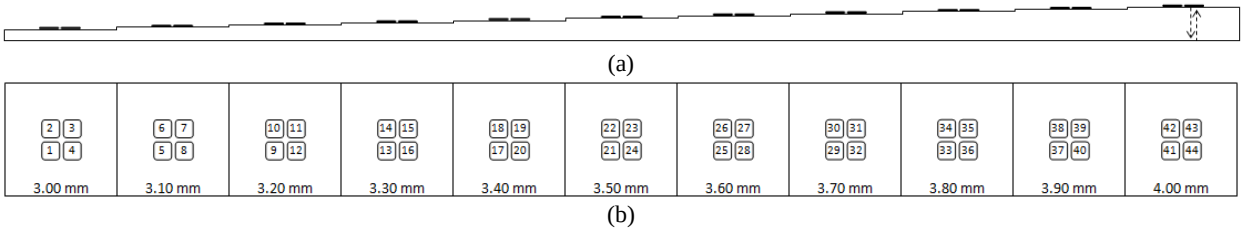

Figure 9. The a) top view and b) side view schematic of a 3-4 mm calibration block with deposited sol-gel sensor elements.

6. MEASUREMENT ACCURACY DATA

The measured thickness values are compared to the calibration block thickness values in Fig. 10 showing eight Peak-to-Peak outliers and one Cross Correlation outlier. All eight Peak-to-Peak outliers coincide with a local second peak with greater absolute amplitude compared to the local first peak; the larger second peak is mistakenly identified resulting in an outlier thickness measurement. These outliers could be avoided by analyzing the rectified signal, calculation method modification, or gate adjustment; although results are presented with and without outliers as a relative comparison. The residual variation appears to be random relative to calibration block thickness. The distribution of residual values can be observed in Fig. 11.

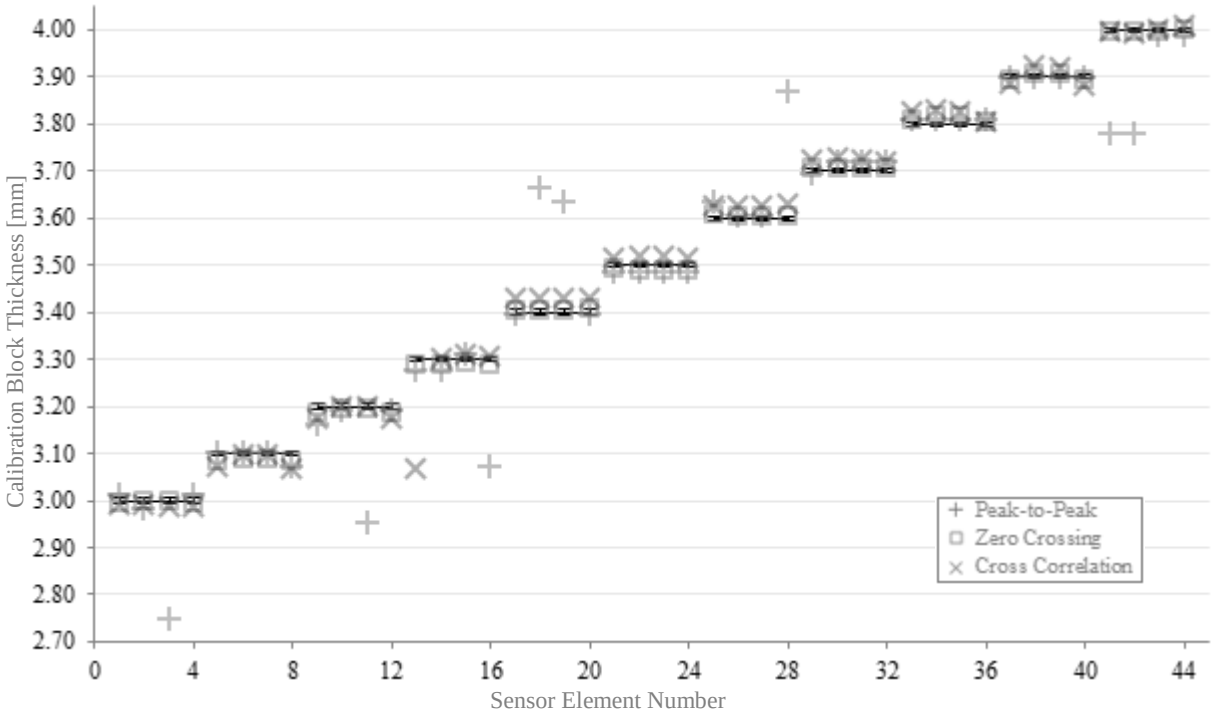

Figure 10. Calculated thickness compared to actual calibration block thickness for each thickness calculation method and for each sensor element.

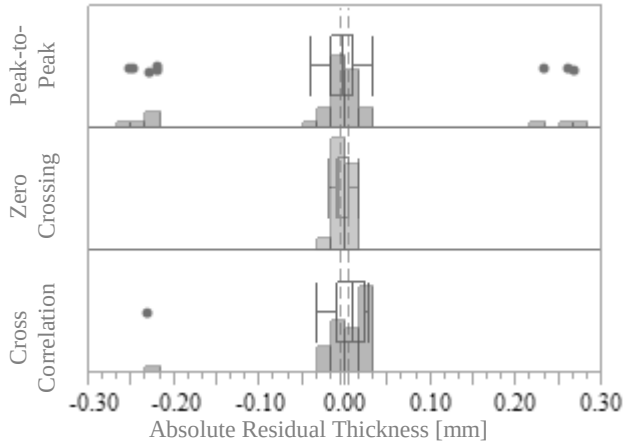

Figure 11. Distribution of residual thickness measurement values for each thickness calculation method.

7. MEASUREMENT ACCURACY RESULTS

A previously described *absolute* residual value analysis[10] approach may be an efficient method to calculate equivalent a_{90} and $a_{90/95}$ accuracy precision values[41] for SHM applications; but this *absolute* residual method does not capture residual asymmetry which may be interesting to understand whether a particular calculation method is more or less likely to under-size or over-size thickness values. A more complete method would be to fit various distribution models to the *true* residual data using a maximum likelihood method to capture any residual asymmetry.

7.1 Relative Likelihood Background

This statistical theory background section is drawn from Meeker and Escobar chapters 2, 4, & 8[42]. In general, given a set of data, likelihood functions can be used to infer the parameters of a statistical model that best represent that particular set of data. A set of likelihood values can be compared for various distribution models over a range of model parameters in attempt to find the model and parameter values that maximize the likelihood function; such model and corresponding parameter values are considered to best represent, or best fit, the data set. The likelihood function is applied to a location scale distribution function using exact observations as shown in Eq. 2 with μ as the location parameter, σ as the scale parameter, f as the probability density function, y as the observed value, and ϕ and Φ as related to the probability density functions and cumulative distribution functions for normal, smallest extreme value (SEV), largest extreme value (LEV), and logistic distributions as described in Eqs. 3-6. The relative likelihood function in Eq. 7 can be used to identify parameter confidence regions with the specific case of a 95% confidence region in Eq. 8.

$$L(\mu,\sigma)=\prod_{i=1}^{n}L_i(\mu,\sigma,data_i)=\prod_{i=1}^{n}f(y_i;\mu,\sigma)=\prod_{i=1}^{n}\left[\frac{1}{\sigma}\phi\left(\frac{y_i-\mu}{\sigma}\right)\right] \tag{2}$$

$$\phi_{nor}(z)=(2\pi)^{-1/2}e^{-z^2/2}\qquad \Phi_{nor}(z)=\int_{-\infty}^{z}\phi_{nor}(w)dw \tag{3}$$

$$\phi_{sev}(z)=e^{(z-e^z)}\qquad \Phi_{sev}(z)=1-e^{-e^z} \tag{4}$$

$$\phi_{lev}(z)=e^{(-z-e^z)}\qquad \Phi_{lev}(z)=e^{-e^{-z}} \tag{5}$$

$$\phi_{logis}(z)=e^z(1+e^z)^{-2}\qquad \Phi_{logis}(z)=e^z(1+e^z)^{-1} \tag{6}$$

$$R(p)=\frac{L(p)}{L(\hat{p})} \tag{7}$$

$$R(\mu,\sigma)>\exp\left(-\chi^2_{(0.95;2)}/2\right)=0.05 \tag{8}$$

7.2 True Residual Results

The specific parametric distribution model and corresponding model parameters with the highest likelihood, or best fit, can be used to calculate the 90% probability range of residual measurement upper and lower confidence bounds to determine an a_{90} value; next, a second distribution model can be generated from the initial best fit distribution model 95% likelihood confidence bound set of potential parameters; finally, this second distribution model can be analyzed to find the 90% probability range of residual measurement upper and lower confidence bounds to determine an $a_{90/95}$ value.

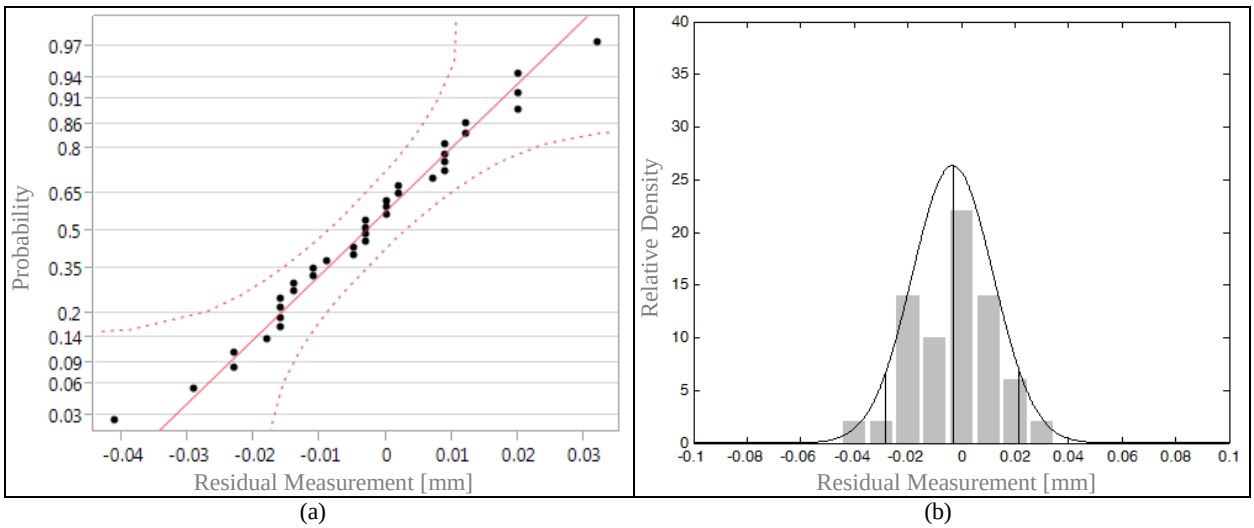

(a) (b)

Figure 12. The maximum likelihood Normal distribution a) linearized cumulative distribution (solid line) fits the data within the normal parametric 95% confidence bounds (dashed lines). The b) probability density function matches the histrogram data; 90% lower confidence bound a_{90L} value of -0.028 mm and upper confidence bound a_{90U} value of 0.022 mm can be observed.

The 4 mm calibration block data set Peak-to-Peak calculation method with outliers removed is used to demonstrate the true residual method. The likelihood and relative likelihood functions for this data set are calculated from Eqs. 2-7.The largest maximum likelihood value observed is from the Normal distribution reported in Table 4 along with the corresponding μ and σ model parameters. The corresponding Normal linearized cumulative distribution function and Normal probability density function are shown to fit the data as observed in Fig. 12. The 90% lower confidence bound a_{90L} value of -0.028 mm and upper confidence bound a_{90U} value of 0.022 mm can be observed in Fig. 12b and reported in Table 4. The conservative value for a_{90} is the absolute maximum a_{90U} or a_{90L} value as reported in Table 4.

The a_{90} values are derived from the most likely distribution model and corresponding most likely distribution model parameters; but a range of potential distribution model parameters are possible due to inherent model lack of fit. The relative likelihood function described in Eqs. 7-8 can be used to establish a 95% confidence region of the potential μ and σ parameter values as shown in Fig. 13 with the 0.05 contour line delineating such a region. The perimeter of this region consists of a set of extreme μ and σ parameter values. The probability density functions generated by a sampling of such extreme μ and σ parameter values are shown in Fig. 14 as grey lines along with the maximum likelihood probability density function as a single black line. A new extreme probability density function can be obtained as the maximum of a sufficient number of probability density functions derived from the parameter set of the confidence region as shown in Fig. 15. The extreme probability density function 90% lower confidence bound $a_{90/95L}$ value of -0.036 mm and upper confidence bound $a_{90/95U}$ value of 0.029 mm can be observed in Fig. 15 and reported in Table 4. The conservative value for $a_{90/95}$ is the absolute maximum $a_{90/95U}$ or $a_{90/95L}$ value as reported in Table 4.

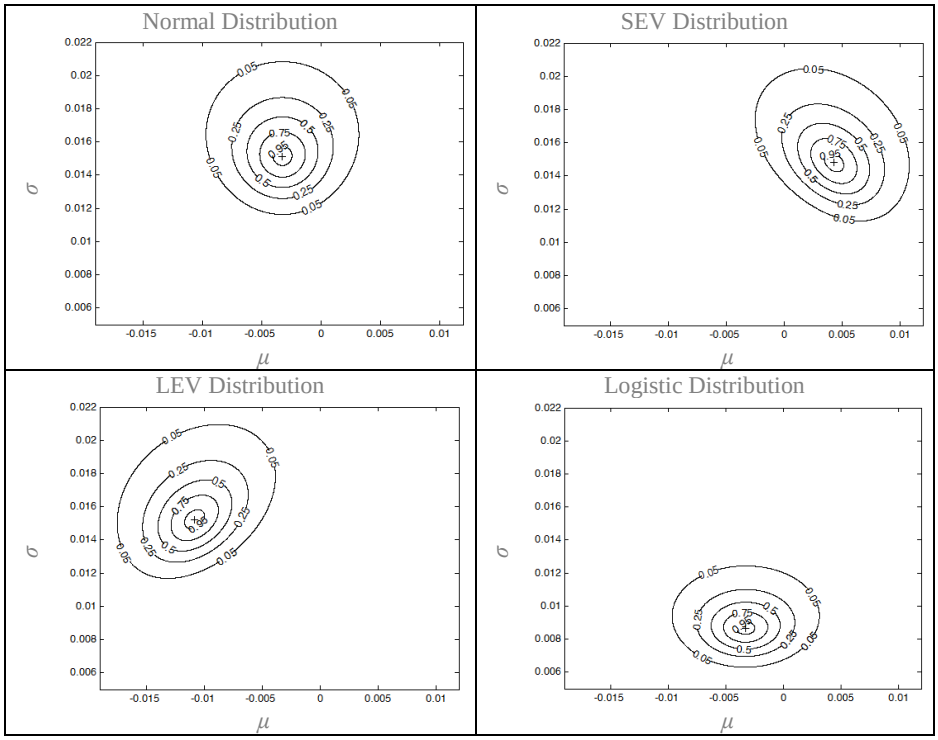

Figure 13. Relative likelihood contour plots with the plus sign as the point of maximum likelihood and the 0.05 contour line outlining the 95% confidence region of the potential μ and σ parameter values.

The total results are reported in Table 4 including the a_{90} and $a_{90/95}$ values for the best fit distribution models for all three thickness calculation methods with and without outlier data points. These results are in an ideal environment at ambient temperature, with a smooth and uniform back-wall reflection surface, and negligible systematic degradation.

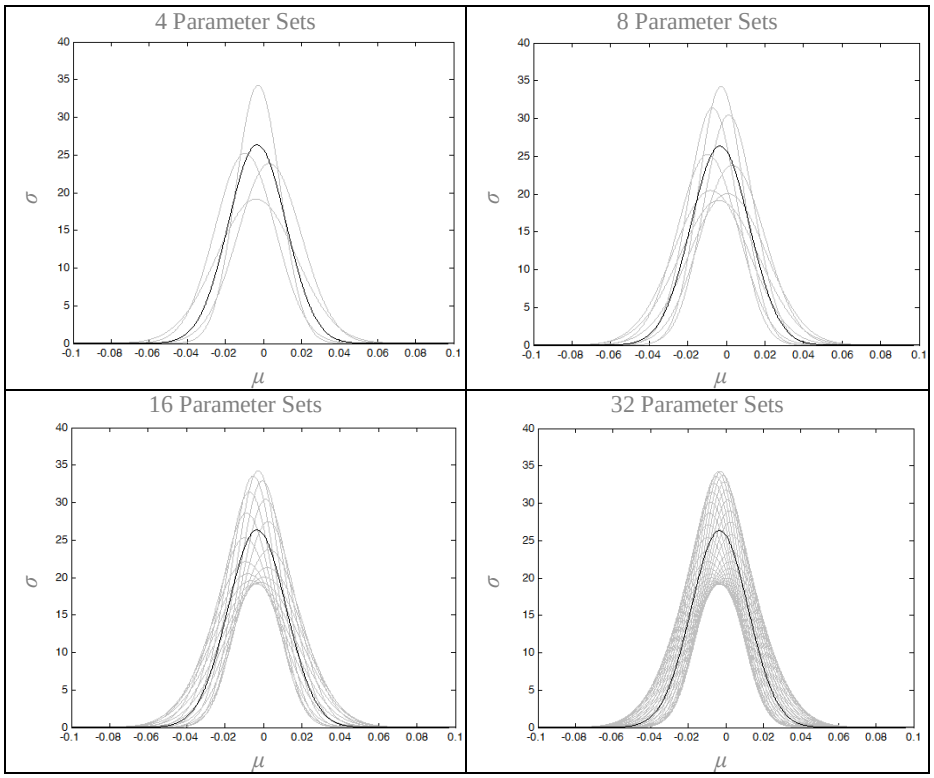

Figure 14. The probability density functions generated by extreme μ and σ parameter values are shown as grey lines along with the maximum likelihood probability density function shown as a single black line.

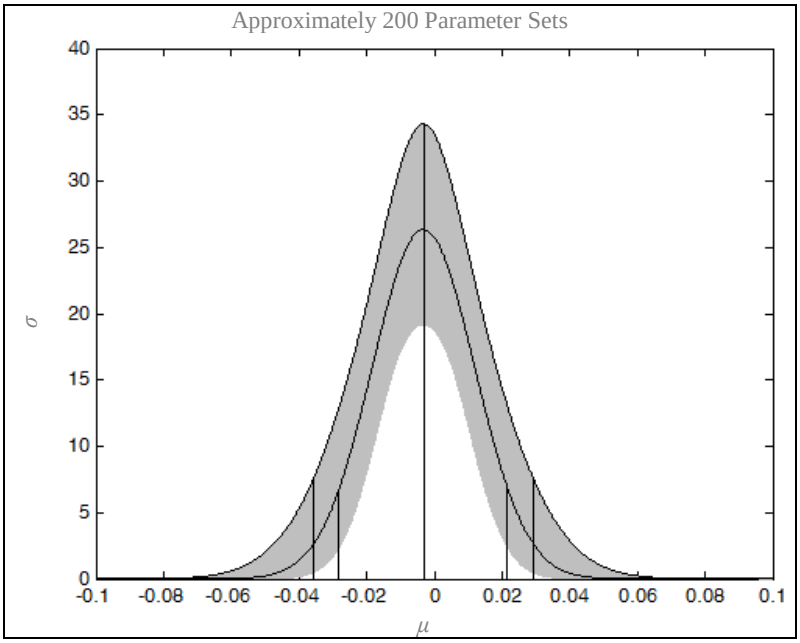

Figure 15. The extreme probability density function is obtained from the maximum of probability density functions derived from the parameter set of the confidence region perimeter; observable as the greater solid black line. The extreme probability density function 90% lower confidence bound $a_{90/95L}$ value of -0.036 mm and upper confidence bound $a_{90/95U}$ value of 0.029 mm can be observed. The original maximum likelihood probability density function can also be observed as the smaller solid black line along with corresponding a_{90L} and a_{90U} values.

Table 4. Results are presented including the a_{90} and $a_{90/95}$ values [mm] for the best fit distribution models for all three thickness calculation methods with and without outlier data points. These results are in an ideal environment at ambient temperature, with a smooth and uniform back-wall reflection surface, and negligible systematic degradation.

Thickness Calculation Method	Outliers Included	Distribution Model	Maximum Loglikelihood	μ	σ	a_{90L}	a_{90U}	a_{90}	$a_{90/95L}$	$a_{90/95U}$	$a_{90/95}$
Peak-to-Peak	Yes	Logistic	42.7	-.008	.0453	-.140	.124	.140	-.173	.156	.173
	No	Normal	99.8	-.003	.0151	-.028	.022	.028	-.036	.029	.036
Zero Crossing	Yes	LEV	146.4	-.007	.008	-.016	.015	.016	-.018	.021	.021
	No	LEV	146.4	-.007	.008	-.016	.015	.016	-.018	.021	.021
Cross Correlation	Yes	SEV	102.3	.013	.018	-.041	.033	.041	-.055	.041	.055
	No	SEV	113.4	.015	.015	-.028	.031	.031	-.038	.036	.038

8. CONCLUSIONS

On the basis of the current assessment, the ability of online measurement technology to characterize non-uniform and localized pitting corrosion degradation at elevated temperatures could be improved. The improved measurement approach should look to incorporate the positive aspects of both SHM (high frequency of measurements for corrosion monitoring) and NDE (inspection of a large area and precise measurements for quantifying the thinnest points in a system). The ultrasonic bulk wave NDE technique is a promising option to directly measure the minimum wall thickness points of a rough and non-uniformly corroded inside pipe wall surface in a high temperature permanent monitoring application. Prior work around the use of thin film sol-gel transducers was identified. New work around the characterization of the elastic wave beam profile from a sol-gel transducer was presented with limited results. Additional work is necessary to optimize the photoelastic visualization system to achieve a lower and more uniform signal-to-noise ratio in the image. Also, a maximum likelihood statistical method was described and applied to quantify the asymmetric measurement accuracy and precision of various thickness calculation methods from a simple experiment in an ideal environment. This statistical method can be applied to quantify the measurement accuracy and precision in more challenging environmental conditions.

ACKNOWLEDGEMENTS

This work supported by BP Products North America and Applus RTD Technological Center in the Netherlands.

REFERENCES

[1] Qing, W., "Processing high TAN crude: part I," Petroleum Technology Quarterly (Q4), 35-43 (2010).
[2] Ropital, F. "Current and future corrosion challenges for a reliable and sustainable development of the chemical, refinery, and petrochemical industries," Materials and Corrosion 60(7), 495-500 (2009).
[3] Slavcheva, E. B., Shone, B. and Turnbull, A., "Review of naphthenic acid corrosion in oil refining," British Corrosion Journal 34(2), 125-131 (1999).
[4] American Petroleum Institute, "API 571 Damage Mechanisms Affecting Fixed Equipment in the Refining Industry," API Publishing Services, Washington, (2011).
[5] Wu, X. Q., Jing, H. M., Zheng, Y. G., Yao, Z. M. and Ke, W., "Study on high-temperature naphthenic acid corrosion and erosion-corrosion of aluminized carbon steel," Journal of Materials Science 39(3), 975-985 (2004).
[6] American Petroleum Institute, "API 579-1/ASME FFS-1 Fitness-For-Service," API Publishing Services, Washington, (2007).
[7] Beissner, R. E. and Birring, A. S. "Nondestructive Evaluation Methods for Characterization of Corrosion: State of the Art Review," Ref# NTIAC-88-1, Nondestructive Testing Information Analysis Center, San Antonio, (1988).
[8] Lozev, M. G., Smith, R. W. and Grimmet, B. B., "Evaluation of methods for detecting and monitoring of corrosion damage in risers," Journal of Pressure Vessel Technology - Transactions of the ASME 127(3), 244-254 (2005).

[9] Liu, Z and Kleiner, Y., "State of the art review of inspection technologies for condition assessment of water pipes," Measurement 46(1), 1-15 (2013).
[10] Eason, T. J., Bond, L. J. and Lozev, M. L., "Structural health monitoring of localized internal corrosion in high temperature piping for oil industry," Proc. 41st Review of Progress in Quantitative NDE 34, Eds. D. E. Chimenti and, L. J. Bond, (Boise, ID, July 2014) AIP Conference Proceedings (2015). [in press]
[11] Bray, D. E. and Stanley, R. K., [Nondestructive Evaluation: A Tool in Design, Manufacturing, and Service], CRC Press - Taylor & Francis Group, Boca Raton, (1997).
[12] ESR Technology Ltd., "The HOIS Interactive Knowledge Base" <http://hois-ikb.esrtechnology.com> (July 2014).
[13] Hansen, P., Alismail, H., Rander, P. and Browning, B., "Pipe mapping with monocular fisheye imagery," Proc. IEEE/RSJ International Conference on Intelligent Robots and Systems, 5180-5185 (2013).
[14] Duran, O., Althoefer, K. and Seneviratne, D., "Automated pipe defect detection and categorization using camera/laser-based profiler and artificial neural network," IEEE Transactions on Automation Science and Engineering 4(1), 118-126 (2007).
[15] Majumder, M., Gangopadhyay, T. K., Chakraborty, A. K., Dasgupta, K. and Bhattacharya, D. K., "Fibre Bragg gratings in structural health monitoring - Present status and applications," Sensors and Actuators A: Physical 147(1), 150-164 (2008).
[16] Tennyson, R. C., Banthia, N., Rivera, E., Huffman, S. and Sturrock, I., "Monitoring structures using long gauge length fibre optic sensors," Canadian Journal of Civil Engineering 34(3), 422-429 (2007).
[17] Barshan, B., "Fast processing techniques for accurate ultrasonic range measurements," Measurement Science and Technology 11(1), 45-50 (2000).
[18] Jarvis, A. J. C. and Cegla, F. B., "Application of the distributed point source method to rough surface scattering and ultrasonic wall thickness measurement," Journal of the Acoustical Society of America 132(3), 1325-1335 (2012).
[19] Rohrback Cosasco Systems, "Ultracorr®-2 Corrosion Monitoring System User Manual," 2012, <http://www.cosasco.com/documents/Ultracorr2_IS_Book_RevB.pdf> (January 2015).
[20] GE Sensing & Inspection Technologies, "Rightrax LT Specifications - Online Corrosion Monitoring System," 2010, <http://www.ge-mcs.com/download/ultrasound/corrosion-monitoring/GEIT-20211EN_rightrax-lt-specifications.pdf.> (April 2014).
[21] GE Sensing & Inspection Technologies, "Rightrax HT Specifications - Online Corrosion Monitoring System," 2009, <http://www.ge-mcs.com/download/ultrasound/corrosion-monitoring/GEIT-20212EN_rightrax-ht-specifications.pdf> (April 2014).
[22] Permasense Limited, "Integrity Monitoring Systems for Enhanced Profitability in Oil & Gas," <http://www.permasense.com/brochure.php> (January 2015).
[23] Cegla, F. B., Cawley, P., Allin, J. and Davies, J., "High-temperature (>500 C) wall thickness monitoring using dry-coupled ultrasonic waveguide transducers," IEEE Transactions on Ultrasonic Ferroelectrics and Frequency Control 58(1), 156-167 (2011).
[24] Barrow, D. A., Petroff, T. E. and Sayer, M., "Method for producing thick ceramic films by a sol gel coating process," United States of America Patent 5585136, (1996).
[25] Kobayashi, M., Jen, C. K., Bussiere, J. F. and Wu, K. T., "High-temperature integrated and flexible ultrasonic transducers for nondestructive testing," NDT & E International 42(2), 157-161 (2009).
[26] Shih, J. L., Kobayashi, M. and Jen, C. K., "Flexible metallic ultrasonic transducers for structural health monitoring of pipes at high temperatures," IEEE Transactions on Ultrasonics, Ferroelectrics, and Frequency Control 57(9), 2103-2110 (2010).
[27] Baborovsky, V. M., Marsh, D. M., Slater, E. A., "Schlieren and computer studies of the interaction of ultrasound with defects," Nondestructive Testing 6(4), 200-207 (1973).
[28] Heidemanm, E. and Hoesch, K. H., "Optical investigations of ultrasonic fields in liquids and glasses," Journal of Physics 104(3-4), 197-206 (1937). German.
[29] Hanstead, P. D., "Ultrasonic visualization," British Journal of Non-Destructive Testing 14(6), 162-169 (1972).
[30] Wyatt, R. C., "Imaging ultrasonic probe beams in solids," British Journal of Non-Destructive Testing 17(5), 133-140 (1975).
[31] Hall, K. G. and Farley, P. G., "An evaluation of ultrasonic probes by the photoelastic visualisation method" British Journal of Non-Destructive Testing 20, 171-184 (1978).
[32] Hall, K. G., "Observing ultrasonic wave propagation by stroboscopic visualization methods," Ultrasonics 20(4), 159-167 (1982).

[33] Ginzel, E. and Stewart, D., "Photo-elastic visualization of phased array ultrasonic pulses in solids," 16th World Conference on Nondestructive Testing, (2004).
[34] Ginzel, E. and Zheng, Z., "Quantification of ultrasonic beams using photoelastic visualization," NDT.net 11(5), (2006).
[35] Schmitte, T., Orth, T. and Kersting, T., "Visualization of phased-array sound fields and flaw interaction using the photoelastic effect," Proc. Review of Progress in Quantitative Nondestructive Evaluation 31(1), AIP Conf. Proc. 1430, 1976-1983 (2012).
[36] Schmitte, T., Orth, T., Spies, M and Kersting, T., "Sound fields of phased array probes: comparison of photoelastic measurements and simulations," DACH Annual Meeting, (2012). German.
[37] Washimori, S., Mihara, T. and Tashiro, H., "Investigation of the sound field of phased array using the photoelastic visualization technique and the accurate FEM," Materials Transactions 53(4), 631-635 (2012).
[38] Eclipse Scientific, "Ultrasonic Photoelastic Visualization System Data Sheet," <http://www.eclipsescientific.com/Products/Training/Photoelastic/ESPhotoElastic%20Data%20Sheet.pdf> (October 2014).
[39] Krautkramer, J. and Krautkramer, H., [Ultrasonic Testing of Materials], Springer-Verlag, New York, (1990).
[40] Deschamps, G. A., "Ray techniques in electromagnetics," Proceedings of the IEEE 60(9), 1022-1035 (1972).
[41] "MIL-HDBK-1823A - Nondestructive Evaluation System Reliability Assessment," Department of Defense - United States of America, Dayton, (2009).
[42] Meeker, W. Q. and Escobar, L. A., [Statistical Methods for Reliability Data], John Wiley & Sons, (1998).